Soft Matter

Accepted Manuscript

ROYAL SOCIETY OF CHEMISTRY

www.rsc.org/softmatter

Journal Name

ARTICLE TYPE

Cite this: DOI: 10.1039/xxxxxxxxxx

Sedimentation equilibria in polydisperse ferrofluids: critical comparisons between experiment, theory, and computer simulation

Ekaterina A. Elfimova,[a] Alexey O. Ivanov,[a] Ekaterina V. Lakhtina,[b] Alexander F. Pshenichnikov,[b] and Philip J. Camp[a,c]

Received Date
Accepted Date

DOI: 10.1039/xxxxxxxxxx

www.rsc.org/journalname

The sedimentation equilibrium of dipolar particles in a ferrofluid is studied using experiment, theory, and computer simulation. A theory of the particle-concentration profile in a dipolar hard-sphere fluid is developed, based on the local-density approximation and accurate expressions from a recently introduced logarithmic free energy approach. The theory is tested critically against Monte Carlo simulation results for monodisperse and bidisperse dipolar hard-sphere fluids in homogeneous gravitational fields. In the monodisperse case, the theory is very accurate over broad ranges of gravitational field strength, volume fraction, and dipolar coupling constant. In the bidisperse case, with realistic dipolar coupling constants and compositions, the theory is excellent at low volume fraction, but is slightly inaccurate at high volume fraction in that it does not capture a maximum in the small-particle concentration profile seen in simulations. Possible reasons for this are put forward. Experimental measurements of the magnetic-susceptibility profile in a real ferrofluid are then analysed using the theory. The concentration profile is linked to the susceptibility profile using the second-order modified mean-field theory. It is shown that the experimental results are not consistent with the sample being monodisperse. By introducing polydispersity in the simplest possible way, namely by assuming the system is a binary mixture, almost perfect agreement between theory and experiment is achieved.

1 Introduction

Sedimentation is a widespread phenomenon in colloidal suspensions. At equilibrium, the gravitational, Brownian, and interaction forces acting on nanoparticles in suspension balance one another out, leading to a stationary particle-concentration profile. In many industrial applications – such as in personal-care products and foodstuffs – sedimentation is something to be avoided, and to this end, the properties of colloidal particles and the suspending molecular liquid can be tuned to minimise the mass-density difference that, through Archimedes' principle, dictates the effective buoyant force. In analytical techniques such as (ultra)centrifugation, the effective gravitational forces are enhanced in order to generate non-uniform concentration profiles, which can be measured directly, for example by using optical methods. Within the local-density approximation (LDA), and by assuming hydrostatic equilibrium, concentration profiles can be inverted to yield osmotic equations of state.[1–4] In the LDA, the local Helmholtz free energy can be determined from expressions for the bulk free energy, but with the local concentration used in place of the bulk concentration. The LDA is expected to hold when the concentration profile varies on length scales much longer than any microscopic structural length scale: for simple colloidal models, such as those based on hard-sphere fluids, the LDA is seen to be reasonably accurate.[2–4] Sedimentation profiles obtained by analytical ultracentrifugation can also be analysed to yield particle-size distributions in polydisperse colloidal suspen-

[a] Institute of Mathematics and Computer Sciences, Ural Federal University, 51 Lenin Avenue, Ekaterinburg 620000, Russia.
[b] Institute of Continuous Media Mechanics, UB RAS, 1 Korolyev Street, Perm 614013, Russia.
[c] School of Chemistry, University of Edinburgh, David Brewster Road, Edinburgh EH9 3FJ, Scotland. E-mail: philip.camp@ed.ac.uk

sions.[5] Sedimentation – or particle settling – is much more complex when the suspended particles and the constituent particles of the suspending medium are of comparable size, and violations of Archimedes' principle can be observed.[6–8]

This work is focused on sedimentation in ferrofluids. Ferrofluids are comprised of magnetic nanoparticles (typically Fe_3O_4), sterically stabilised with adsorbed surfactant molecules (e.g., oleic acid, oleylamine), and suspended in an inert carrier liquid such as decalin or kerosene. Ferrofluids are highly functional materials, with dynamic, optical, and magnetic properties that can be controlled with external magnetic fields.[9] Magnetic nanoparticles can also be surface-functionalised for use in targeted drug delivery, tumor detection, and tumor destruction through hyperthermia.[10] Sedimentation profiles of dilute suspensions of single-domain magnetite nanoparticles have been determined by ultracentrifugation, and evidence has been found for dimer formation driven by the anisotropic dipolar interactions between the particles.[11] Luigjes *et al.* recently measured concentration profiles in centrifuged monodisperse ferrofluids using optical methods, and inverted the profiles to yield equations of state up to volume fractions $\varphi \simeq 0.12$.[12,13] The equations of state were fitted with theoretical expressions for dipolar hard-sphere (DHS) fluids to yield the apparent dipolar coupling constant, $\lambda \simeq 2$.[13,14] Pshenichnikov *et al.* developed expressions for the concentration profiles in ferrofluids using various approximations for the local thermodynamic properties based on thermodynamic perturbation theory, and various types of fitting to simulation data.[15,16] While sedimentation is of intrinsic interest, it can also be used to drive self-assembly of magnetic nanoparticles in to interesting crystal structures.[17]

In this work, sedimentation in ferrofluids is studied systematically using results based on the LDA and an accurate representation of the Helmholtz free energy, called logarithmic free energy (LFE) theory.[14,18–20] In this approach, the virial expansion of the Helmholtz free energy is recast as the logarithm of another expansion. In this way, the expression for the Helmholtz free energy is less sensitive to series truncation, since the logarithm generates terms of all orders upon Maclaurin expansion. The LFE theory has been thoroughly tested against accurate simulation results for the thermodynamic properties of monodisperse DHS fluids with and without applied fields,[14,18] bidisperse DHS fluids,[19] and the Stockmayer fluid in an applied field.[20] Here, the LFE theory is tested against new Monte Carlo (MC) simulation results for the concentration profiles in monodisperse and bidisperse DHS fluids. Then, the LFE theory is used to analyse a concentration profile determined in experiments from local magnetic-susceptibility measurements. It is demonstrated that polydispersity is a crucial element of the analysis, in that it is impossible to describe the experimentally determined magnetic-susceptibility profile using a monodisperse model. As a minimum, a bidisperse model is required to describe the experimental results. This is an important step, because almost all real ferrofluids have considerable polydispersity, and this can have pronounced effects on the magnetic and structural properties.[21–30]

This article is organised as follows. In Section 2 the experimental measurements are described, and the models and corresponding theoretical and simulation methods are detailed. Section 3 begins with a thorough comparison of the theory with simulation results, and ends with an analysis of an experimentally measured concentration profile. The conclusions are presented in Section 4.

2 Models and methods

2.1 Experimental

A ferrofluid comprising magnetite particles sterically stabilised with oleic acid and suspended in kerosene was prepared by the standard method of chemical precipitation.[9] The mass density of the sample was 950 kg m^{-3}: using the (bulk) densities of magnetite (5200 kg m^{-3}) and kerosene (790 kg m^{-3}), and assuming that the mass density of the oleic-acid layer is similar to that of kerosene, the apparent magnetic volume fraction is $\Phi^{\rm m} = 0.036$. The static magnetic susceptibility of the original homogeneous suspension at $T = 295$ K was $\chi = 0.490$. The ferrofluid was poured in to a glass capillary of length of $L_z = 60$ mm and inner diameter 2 mm, and the end of the capillary was sealed. The capillary was placed in a centrifuge at an angle of 42° to the horizontal. The horizontal distance between the top of the capillary and the centrifuge rotor was $r_0 = 40$ mm, so that the radius of rotation at height z, measured along the capillary from the bottom, was $r(z) = [r_0 + (L_z - z)\cos 42°]$. The centrifugal acceleration was $\omega^2 r(z)$, where ω is the angular velocity. The projection of the centrifugal acceleration along the capillary was therefore

$$g_{\rm c}(z) = \omega^2 r(z)\cos 42° \qquad (1)$$

which was the effective position-dependent gravitational acceleration in the centrifuge. Taking a typical rotation speed of $\omega = 65$ rad s^{-1}, the gravitational accelerations at the top ($z = L_z$), centre ($z = L_z/2$), and bottom ($z = 0$) of the capillary were approximately 13 g, 20 g, and 27 g, respectively (with $g = 9.807$ m s^{-2}). The centrifuge was switched on and off several times during the experiment, with the duration of each stage ranging from 30 to 180 minutes, all carried out over a period of about $1\frac{1}{2}$ days. At the end of each stage, the local initial magnetic susceptibility of the ferrofluid $\chi(z)$ was measured along the length of the capillary at $T = 295$ K. As shown in Section 3.2, these measurements can be analysed in combination with theory to yield the sedimentation profile, since the magnetic susceptibility of a ferrofluid depends on the particle concentration uniquely. To measure the local magnetic susceptibility, the capillary was carefully removed from the centrifuge and drawn through the measuring coil of a mutual in-

ductance bridge. The design of a mutual inductance bridge was reported in Ref.[31], but in this work a simplified version was used. A peculiarity of this bridge design is a miniature measuring coil of length 2 mm, which defines the spatial resolution of the device, since the output signal corresponds to the magnetic susceptibility averaged over the volume of the measuring coil. The measured values of susceptibility were assigned to the mid-point of the measuring coil.

Measurements were conducted at a field frequency of 4 kHz. Low-frequency measurements are subject to high signal-to-noise ratios, while high-frequency measurements may exclude the contributions from large particles and aggregates with long reorientational relaxation times. The chosen frequency represents a compromise whereby small and medium-sized particles can 'follow the field' in quasi-equilibrium, i.e., the field frequency is much smaller than the resonance, absorption frequency. For large-sized particles, this condition may be violated. A comparison of the results with existing data on the low-frequency susceptibility of magnetite colloids[32] suggests that the concentration of large-sized particles determined from the magnetic susceptibility in this way can be underestimated by approximately 20–30%.

Figure 1 shows the measurements of the magnetic-susceptibility profile $\chi(z)$ taken at various time intervals. $\chi(z)$ varies very little between 29 and 38 hours, and so it can be assumed that thermodynamic equilibrium has been established by this time. In Section 3.2, only the profile measured after 38 hours is analysed with theory.

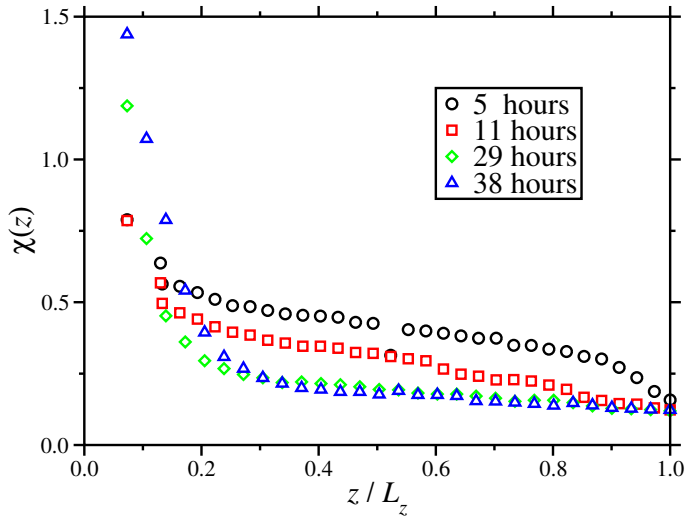

Fig. 1 Experimental measurements of the magnetic-susceptibility profile $\chi(z)$ taken after 5, 11, 29, and 38 hours. The capillary length $L_z = 60$ mm, and the spatial resolution is 2 mm.

2.2 Monodisperse model

The magnetic nanoparticles are modeled as dipolar hard spheres, with magnetic-core diameter x, surfactant layer thickness δ, and overall diameter $\sigma = x + 2\delta$. The magnetic dipole moment on a particle is $\mathbf{m}$, and $m = |\mathbf{m}| = M_s v_m$ where M_s is the saturation magnetization density of the core material, and $v_m = \pi x^3/6$ is the magnetic-core volume. The pair interaction energy between particles i and j is

$$u_{ij} = \begin{cases} \infty & r_{ij} < \sigma \\ \dfrac{\mu_0}{4\pi}\left[\dfrac{(\mathbf{m}_i\cdot\mathbf{m}_j)}{r_{ij}^3} - \dfrac{3(\mathbf{m}_i\cdot\mathbf{r}_{ij})(\mathbf{m}_j\cdot\mathbf{r}_{ij})}{r_{ij}^5}\right] & r_{ij} \geq \sigma \end{cases} \quad (2)$$

where μ_0 is the vacuum magnetic permeability, $\mathbf{r}_{ij}$ is the interparticle separation vector, and $r_{ij} = |\mathbf{r}_{ij}|$. The total potential energy of N particles in a uniform gravitational field acting in the z direction is

$$U = \sum_{i=1}^{N-1}\sum_{j=i+1}^{N} u_{ij} + \sum_{i=1}^{N} v_m \Delta\rho g_c z_i \quad (3)$$

where $\Delta\rho > 0$ is the difference in mass densities between the particle core and the suspending liquid, and g_c is the gravitational acceleration. Note that in a centrifuge, the gravitational acceleration is a function of position, as defined in eqn. (1): the model is extended to a non-uniform field by inserting the appropriate function $g_c(z)$. The magnetic-core volume is used here because in typical systems, the mass density of the surfactant layer including any penetrating carrier-liquid molecules is similar to that of the bulk carrier liquid. The strengths of the gravitational and dipolar energies are specified by a gravitational parameter G and the dipolar coupling constant $\lambda = \mu_0 m^2/4\pi k_B T\sigma^3$, respectively. G is the inverse of the gravitational length, and is given by

$$G = \frac{v_m \Delta\rho g_c}{k_B T} \quad (4)$$

where k_B is Boltzmann's constant, and T is the temperature. For non-interacting particles in a uniform gravitational field [G = constant] the local number concentration is given directly by the Boltzmann distribution

$$c(z) = \frac{NG}{A}\exp(-Gz) = nG\exp(-Gz) \quad (5)$$

where A is the cross-sectional area of the container, and $n = N/A$ is the surface concentration. It is convenient to specify the height of the container L_z and hence define an overall volume fraction of particles in the container. This is given by

$$\Phi = \frac{nv}{L_z} \quad (6)$$

where $v = \pi\sigma^3/6$ is the total volume of a particle. Since $c(z)$ is a measure of the probability of finding a particle at height z, the average volume fraction in the sedimentation profile (as opposed

to within the container) is given by

$$\langle\varphi\rangle = \frac{\int_0^{L_z} c(z)\varphi(z)\,\mathrm{d}z}{\int_0^{L_z} c(z)\,\mathrm{d}z} \tag{7}$$

where $\varphi(z) = c(z)v$ is the local volume fraction. As long as $c(z)$ decays to zero near $z = L_z$, this does not depend on the height of the container used. An effective layer thickness can be identified with the average

$$\langle z\rangle = \frac{\int_0^{L_z} c(z)z\,\mathrm{d}z}{\int_0^{L_z} c(z)\,\mathrm{d}z}. \tag{8}$$

In the case of non-interacting particles in a uniform gravitational field, $\langle\varphi\rangle = nvG/2 = \Phi GL_z/2$ and $\langle z\rangle = 1/G$.

2.3 Bidisperse model

In the bidisperse fluid, there are small (s) particles and large (l) particles with magnetic-core diameters x_s and x_l, and hard-sphere diameters $\sigma_\mathrm{s} = x_\mathrm{s} + 2\delta$ and $\sigma_\mathrm{l} = x_\mathrm{l} + 2\delta$. Separate dipolar coupling constants $\lambda_\alpha = \mu_0 m_\alpha^2/4\pi k_\mathrm{B}T\sigma_\alpha^3$, gravitational parameters G_α, particle volumes $v_\alpha = \pi\sigma_\alpha^3/6$, surface concentrations n_α, overall (magnetic) volume fractions $\Phi_\alpha^{(\mathrm{m})}$, concentration profiles $c_\alpha(z)$, and volume-fraction profiles $\varphi_\alpha(z) = c_\alpha(z)v_\alpha$ are assigned to species $\alpha = \mathrm{s,l}$. Averages for each species ($\langle\varphi\rangle_\alpha$, $\langle z\rangle_\alpha$) are calculated from its own concentration profile $c_\alpha(z)$, and total averages ($\langle\varphi\rangle$, $\langle z\rangle$) are calculated from the total concentration profile $c(z) = c_\mathrm{s}(z) + c_\mathrm{l}(z)$ according to eqns. (7) and (8). The total average height is simply a weighted sum of the individual averages:

$$\langle z\rangle = \frac{n_\mathrm{s}\langle z\rangle_\mathrm{s} + n_\mathrm{l}\langle z\rangle_\mathrm{l}}{n_\mathrm{s} + n_\mathrm{l}}. \tag{9}$$

$\langle\varphi\rangle$ is a more complicated function of the individual-species averages:

$$\langle\varphi\rangle = \frac{n_\mathrm{s}\langle\varphi\rangle_\mathrm{s} + n_\mathrm{l}\langle\varphi\rangle_\mathrm{l}}{n_\mathrm{s} + n_\mathrm{l}} + \left(\frac{v_\mathrm{s} + v_\mathrm{l}}{n_\mathrm{s} + n_\mathrm{l}}\right)\int_0^\infty c_\mathrm{s}(z)c_\mathrm{l}(z)\,\mathrm{d}z. \tag{10}$$

2.4 Theory

The sedimentation profile is determined from the equilibrium condition that the sedimentation flux cancels out the diffusive flux.[15,33] For a monodisperse fluid, the sedimentation flux at height z is

$$-\frac{c(z)K(c)v_\mathrm{m}\Delta\rho g_\mathrm{c}}{3\pi\eta\sigma} \tag{11}$$

where $K(c)$ is the relative mobility as compared to low particle concentration, and η is the viscosity of the carrier liquid. The diffusive flux according to Fick's law is

$$-\frac{c(z)K(c)D_0}{k_\mathrm{B}T}\left(\frac{\partial\mu}{\partial z}\right) \tag{12}$$

where $D_0 = k_\mathrm{B}T/3\pi\eta\sigma$ is the single-particle diffusion coefficient at low concentration. At equilibrium, the two fluxes cancel each other out, leading to the relation

$$-G = \frac{1}{k_\mathrm{B}T}\left(\frac{\partial\mu}{\partial z}\right) = \frac{1}{k_\mathrm{B}T}\left(\frac{\partial\mu}{\partial\varphi}\right)\frac{\mathrm{d}\varphi}{\mathrm{d}z}. \tag{13}$$

Integrating this expression gives

$$-\int_0^z G\,\mathrm{d}z = \frac{1}{k_\mathrm{B}T}\int_{\varphi(0)}^{\varphi(z)}\left(\frac{\partial\mu}{\partial\varphi}\right)\mathrm{d}\varphi \tag{14}$$

where $\varphi(0)$ is fixed by the requirement that $L_z^{-1}\int_0^{L_z}\varphi(z)\mathrm{d}z = \Phi$. Note that in a centrifuge, G depends on position as defined in eqns. (1) and (4). In a bidisperse fluid, the same development leads to two coupled differential equations analogous to eqn. (13), to be solved subject to the overall specified volume fractions of small and large particles, Φ_s and Φ_l.

$$\begin{cases} -G_\mathrm{s} = \dfrac{1}{k_\mathrm{B}T}\displaystyle\sum_{\alpha=\mathrm{s,l}}\left(\frac{\partial\mu_\mathrm{s}}{\partial\varphi_\alpha}\right)\frac{\mathrm{d}\varphi_\alpha}{\mathrm{d}z} \\ -G_\mathrm{l} = \dfrac{1}{k_\mathrm{B}T}\displaystyle\sum_{\alpha=\mathrm{s,l}}\left(\frac{\partial\mu_\mathrm{l}}{\partial\varphi_\alpha}\right)\frac{\mathrm{d}\varphi_\alpha}{\mathrm{d}z} \end{cases} \tag{15}$$

Equations (13) and (15) require the chemical potential of each species as input. There are several routes to explicit expressions for the thermodynamic properties of DHS fluids, including integral-equations (with the mean-spherical approximation) and thermodynamic perturbation theories.[33–39] In this work, the local chemical potentials are derived within the LDA from the logarithmic free energy (LFE) theory.[14,18–20] In the LFE theory, the free energy for the bidisperse fluid is written[19]

$$\frac{F}{Nk_\mathrm{B}T} = \frac{F^\mathrm{HS}}{Nk_\mathrm{B}T} - \ln\left(1 + \sum_{n=1}^\infty n^{-1}I_{n+1}\varphi^n\right) \tag{16}$$

where F^HS is the free energy of the binary hard-sphere mixture, including the ideal-gas terms. This is conveniently obtained from the equation of state by Mansoori *et al.*,[40] which reduces to the Carnahan-Starling equation of state in the monodisperse case.[41] The expansion coefficients I_n represent deviations from the non-polar binary hard-sphere mixture, and each is related to the difference between the normal DHS and HS virial coefficients $\Delta B_i = B_i - B_i^\mathrm{HS}$ ($i \le n$) so as to match the perturbed virial expansion of the free energy[42–46]

$$\frac{F}{Nk_\mathrm{B}T} = \frac{F^\mathrm{HS}}{Nk_\mathrm{B}T} + \sum_{n=1}^\infty n^{-1}\Delta B_{n+1}\varphi^n. \tag{17}$$

The first two relations are $I_2 = -\Delta B_2$ and $I_3 = -\Delta B_3 + \Delta B_2^2$. In Ref.[19], the appropriate expressions for I_2 and I_3 for binary mixtures of DHSs were determined as expansions in the dipolar coupling constants with terms of up to λ^4 and λ^3, respectively. All

thermodynamic properties follow from eqn. (16), and in particular, $\mu_\alpha = (\partial F/\partial N_\alpha)_{N_\beta,V,T}$.

2.5 Computer simulations

In order to test the theory outlined above, Monte Carlo (MC) simulations were used to generate the concentration profiles in the monodisperse and bidisperse models with a uniform gravitational field [G = constant]. Five sets of runs were carried out: (i) monodisperse particles with $G\sigma = 0.05$, $\Phi = 0.050$, and $\lambda = 0$–3; (ii) monodisperse particles with $G\sigma = 0.05$, $\Phi = 0.100$, and $\lambda = 0$–3; (iii) monodisperse particles with $G\sigma = 0.25$, $\Phi = 0.075$, and $\lambda = 0$–4; (iv) bidisperse particles with $\sigma_l/\sigma_s = 1.25$, $G_s\sigma_s = 0.05$, $\lambda_s = 1$, $\Phi = 0.0500$, and $\Phi_s = 0.0350$, 0.0400, 0.0450, and 0.0475; (v) bidisperse particles with $\sigma_l/\sigma_s = 1.25$, $G_s\sigma_s = 0.05$, $\lambda_s = 1$, $\Phi = 0.100$, and $\Phi_s = 0.0700$, 0.0800, 0.0900, and 0.0950. In all cases, the nominal surfactant-layer thickness was set to $\delta = 0$, meaning that $x_\alpha = \sigma_\alpha$, and $\lambda_l/\lambda_s = G_l/G_s = (\sigma_l/\sigma_s)^3$. The choice of $\sigma_l/\sigma_s = 1.25$ therefore gives $\lambda_l/\lambda_s = G_l/G_s = 1.953$.

MC simulations were carried out in the canonical (NVT) ensemble with $N = 2000$ particles. The cuboidal simulation box had a square cross-section in the xy plane, and height in the z direction equal to L_z. Periodic boundary conditions and the minimum-image convention were applied only in the xy direction. In simulations with $G\sigma = 0.05$, the z coordinates of the particles were restricted to $0 \le z \le L_z$. This causes anomalous ordering of the particles near $z = 0$, but because the depth of the fluid layer ($\sim 1/G$) is large in this case, the effects on the sedimentation profile are insignificant. In simulations with $G\sigma = 0.25$, the depth of the layer is much smaller, and the structure near the lower boundary is significant. To counter this, the simulation box was extended to $-L_z \le z \le L_z$, and the gravitational potential energy was $v_m\Delta\rho g_c|z|$. In this way, two sedimentation profiles are in contact with one another, particles can pass through the $z = 0$ plane, and anomalous ordering near $z = 0$ is largely eliminated. Simulation runs of up to 10^9 attempted MC moves per particle were required to reach equilibration, especially with the smaller value of G. Production runs consisted of 10^8 attempted MC moves.

3 Results

The results are presented in two separate sections: in Section 3.1, the theory is tested critically against simulation data for well-defined monodisperse and bidisperse DHS systems; in Section 3.2, the theory is used to analyse experimental data, with an emphasis on the importance of taking particle-size polydispersity into account.

3.1 Comparison between theory and simulation

Figure 2 shows the sedimentation profiles of monodisperse DHSs with constant gravitational parameter $G\sigma = 0.05$, $L_z = 200\sigma$, overall volume fraction $\Phi = 0.050$, and dipolar coupling constants $\lambda = 0$, 1, 2, and 3, calculated from MC simulations and from theory. The initial rise in $\varphi(z)$ near $z = 0$ from simulations is an artifact of using a hard bottom wall. With increasing λ, the fluid layer becomes more compact due to stronger cohesive interactions between the particles. The agreement between $\varphi(z)$ from simulations and theory is very good.

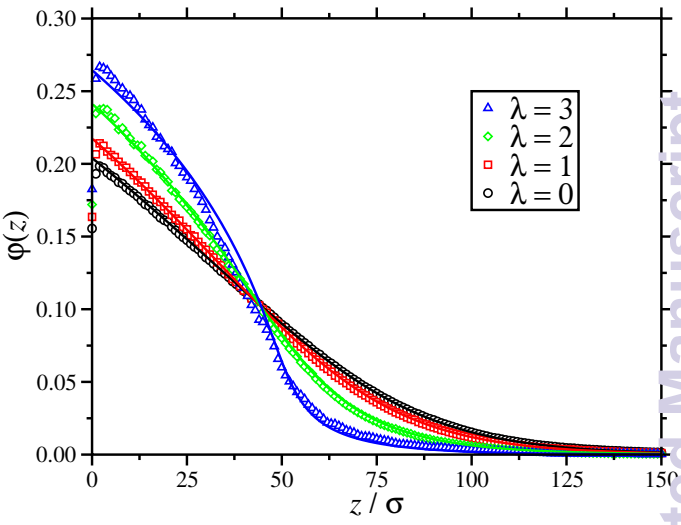

Fig. 2 Sedimentation profiles for monodisperse fluids with constant gravitational parameter $G = 0.05\sigma^{-1}$, $L_z = 200\sigma$, overall volume fraction $\Phi = 0.050$, and dipolar coupling constants $\lambda = 0$ (black circles/line), 1 (red squares/line), 2 (green diamonds/line), and 3 (blue triangles/line). The points are from MC simulations and the lines are from theory.

The agreement is quantified in Table 1 which shows the average properties of the fluid layer. $\langle\varphi\rangle$ defined in eqn. (7) is the average volume fraction of the layer, and this increases by about 50% over the range $\lambda = 0$–3. $\langle z\rangle$ defined in eqn. (8) is the average particle height within the layer, and this decreases by about 30% over the same range of λ. The agreement between these quantities from simulation and theory is excellent.

Figure 3 shows $\varphi(z)$ for the same monodisperse system but at a higher overall volume fraction of $\Phi = 0.100$. The fluid layer again becomes more compact with increasing λ, but to a lesser extent than at $\Phi = 0.050$. The averages $\langle\varphi\rangle$ and $\langle z\rangle$ in Table 1 reflect the densification of the fluid layer, and as before, the agreement between simulation and theory is excellent.

In earlier works, simulations and theory have been compared for dipolar fluids with significantly higher gravitational parameters G.[15,16] For instance, in Ref.[16] monodisperse dipolar soft-sphere fluids were studied under conditions equivalent to $L_z = 20\sigma$, $\Phi = 0.150$, $\lambda = 0$–4, and $G\sigma = 0.25$. With low values of λ, the thickness of the fluid layer was comparable to the box height L_z, and renormalization corrections had to be applied to account for the anomalous ordering of the particles near the bottom of

Table 1 Average properties of sedimentation profiles for monodisperse fluids. G is the gravitational parameter, λ is the dipolar coupling constant, and L_z is the height of the container. Φ, $\langle\varphi\rangle$, and $\langle z\rangle$ are, respectively, the overall volume fraction, the average volume fraction in the profile, and the average height. Results are shown from MC simulations and from theory. The number of particles used in the MC simulations is $N = 2000$ in each case.

$G\sigma$	λ	L_z/σ	Φ	$\langle\varphi\rangle$		$\langle z\rangle/\sigma$	
				MC	theory	MC	theory
0.05	0	200	0.050	0.127	0.128	35.4	35.5
0.05	1	200	0.050	0.136	0.137	32.9	33.2
0.05	2	200	0.050	0.158	0.158	28.3	28.9
0.05	3	200	0.050	0.186	0.189	24.3	23.9
0.05	0	200	0.100	0.186	0.187	47.8	47.9
0.05	1	200	0.100	0.198	0.198	44.9	45.1
0.05	2	200	0.100	0.220	0.219	40.4	40.9
0.05	3	200	0.100	0.237	0.244	37.7	36.8
0.25	0	40	0.075	0.161	0.161	7.9	8.4
0.25	1	40	0.075	0.171	0.171	7.4	7.9
0.25	2	40	0.075	0.195	0.193	6.5	7.0
0.25	3	40	0.075	0.227	0.220	5.5	6.1
0.25	4	40	0.075	0.260	0.248	4.7	5.6

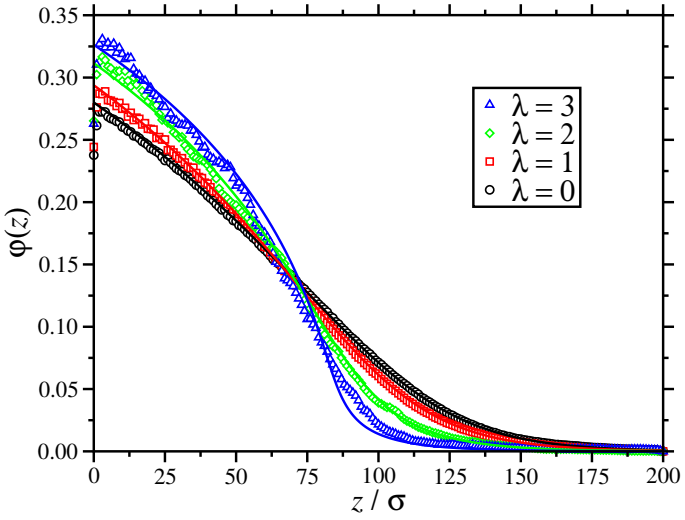

Fig. 3 Sedimentation profiles for monodisperse fluids with constant gravitational parameter $G = 0.05\sigma^{-1}$, $L_z = 200\sigma$, overall volume fraction $\Phi = 0.100$, and dipolar coupling constants $\lambda = 0$ (black circles/line), 1 (red squares/line), 2 (green diamonds/line), and 3 (blue triangles/line). The points are from MC simulations and the lines are from theory.

the box. To reduce these problems, simulations have been repeated with $L_z = 40\sigma$ and $\Phi = 0.075$, and by using the two-profile trick described in Section 2.5. Figure 4 shows the results from simulation and theory, with no corrections or fitting parameters required. The simulation results near $z = 0$ are smooth, showing that bottom-wall artifacts have been eliminated. With $\lambda = 0$–3 the agreement between simulation and theory is excellent. There are substantial deviations with $\lambda = 4$, which probably arises from the onset of strong particle association to form chains, the truncation of the virial coefficients at quite low orders in λ, and the numerical difficulty of integrating the governing differential equation in the theory. In any case, $\lambda = 4$ is an extreme case, and one not often encountered in real ferrofluids. Generally, the agreement between simulation and theory is excellent, and this is reflected in the averages $\langle\varphi\rangle$ and $\langle z\rangle$ presented in Table 1. Overall, it appears that the LDA holds true, even in this quite extreme case.

Figure 5 shows sedimentation profiles for bidisperse DHS fluids with particle-diameter ratio $\sigma_l/\sigma_s = 1.25$, constant small-particle gravitational parameter $G_s\sigma_s = 0.05$, $L_z = 200\sigma_s$, small-particle dipolar coupling constant $\lambda_s = 1$ and overall volume fraction $\Phi = 0.0500$. Four different compositions are considered, with overall small-particle volume fractions $\Phi_s = 0.0350$, 0.0400, 0.0450, and 0.0475. The small-particle, large-particle, and total volume-fraction profiles are shown in each case. The results show that the large-particle profile decays more rapidly than the small-particle profile, reflecting the different gravitational parameters. The curvatures of the profiles are different: $\varphi_l(z)$ is convex over the entire range of z, but $\varphi_s(z)$ is concave near $z = 0$. This is due to the large particles squeezing out the small particles from the bottom of the container. The total profile $\varphi(z)$ is of course just a sum of the two.

The theoretical results in Table 2 show that with an increasing proportion of small particles (increasing Φ_s), the individual averages for the small and large particles change in opposite ways: for the large particles, $\langle\varphi\rangle_l$ decreases and $\langle z\rangle_l$ increases, while for the small particles, $\langle\varphi\rangle_s$ increases and $\langle z\rangle_l$ decreases. With a high value of Φ_l, the large particles settle at the bottom of the container, stabilised by both the high value of G_l and the strong cohesive interactions between the particles. The large particles therefore squeeze out some of the small particles. As a result, when Φ_s is increased, the small particles replace the large particles near the bottom of the container, with a concomitant increase in average volume fraction and decrease in average height. The total average height $\langle z\rangle$ is a simple average of $\langle z\rangle_s$ and $\langle z\rangle_l$, and the total average volume fraction $\langle\varphi\rangle$ shows a slight decrease with increasing Φ_s, and ultimately must converge with $\langle\varphi\rangle_s$ as $\Phi_s \to \Phi$. Overall, the agreement between simulation and theory is very good.

Figure 6 shows results for the same bidisperse system but at a higher overall volume fraction of $\Phi = 0.1000$. There are substantial qualitative differences between the small-particle and large-particle volume-fraction profiles from simulations. $\varphi_s(z)$ shows a local maximum at around $z \simeq 10$–$30\sigma_s$, and $\varphi_l(z)$ rises sharply below this position. This is due to the large particles displacing the small particles from the bottom of the container. The theory describes the individual profiles extremely well above the position of the maximum in $\varphi_s(z)$, and gives a complete description of the total profile $\varphi(z)$, but it does not reproduce the small-z behaviour very well. The reason for this failure cannot be due to the approximate expressions for the virial coefficients, because

Table 2 Average properties of sedimentation profiles for bidisperse fluids with particle-diameter ratio $\sigma_l/\sigma_s = 1.25$, constant small-particle gravitational parameter $G_s = 0.05\sigma_s^{-1}$, and small-particle dipolar coupling constant $\lambda_s = 1$. The box length $L_z = 200\sigma_s$ in each case. Φ_α, $\langle\varphi\rangle_\alpha$, and $\langle z\rangle_\alpha$ are, respectively, the overall volume fraction, the average volume fraction in the profile, and the average height of species $\alpha = s, l$; Φ, $\langle\varphi\rangle$, and $\langle z\rangle$ are the corresponding total values including both species. Results are shown from MC simulations and from theory. N_s and N_l are, respectively, the number of small and large particles used in the MC simulations.

Φ_s	Φ_l	Φ	$\langle\varphi\rangle_s$		$\langle\varphi\rangle_l$		$\langle\varphi\rangle$		$\langle z\rangle_s$		$\langle z\rangle_l$		$\langle z\rangle$		N_s	N_l
			MC	theory	MC	theory	MC	theory	MC	theory	MC	theory	MC	theory		
0.0350	0.0150	0.0500	0.092	0.093	0.078	0.073	0.150	0.151	34.1	33.1	17.5	17.8	31.1	30.3	1640	360
0.0400	0.0010	0.0500	0.106	0.108	0.053	0.048	0.145	0.146	33.7	32.8	17.2	18.1	31.8	31.1	1773	227
0.0450	0.0050	0.0500	0.121	0.122	0.028	0.023	0.140	0.141	33.5	32.5	16.5	19.1	32.5	31.8	1892	108
0.0475	0.0025	0.0500	0.128	0.130	0.013	0.011	0.138	0.139	33.3	32.4	17.4	19.9	32.9	32.1	1948	52
0.0700	0.0300	0.1000	0.133	0.134	0.132	0.100	0.213	0.212	48.3	46.0	20.9	26.3	43.3	42.5	1640	360
0.0800	0.0200	0.1000	0.153	0.156	0.101	0.065	0.207	0.207	47.2	45.2	18.5	26.9	44.0	43.2	1773	227
0.0900	0.0100	0.1000	0.175	0.177	0.064	0.031	0.203	0.202	46.1	44.6	15.9	28.4	44.4	43.7	1892	108
0.0950	0.0050	0.1000	0.185	0.188	0.047	0.015	0.200	0.200	45.7	44.4	11.1	29.4	44.8	44.0	1948	52

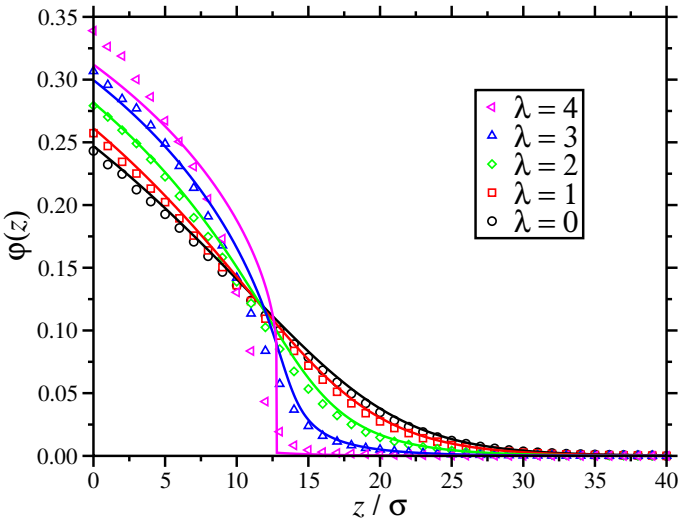

Fig. 4 Sedimentation profiles for monodisperse fluids with constant gravitational parameter $G = 0.25\sigma^{-1}$, $L_z = 40\sigma$, overall volume fraction $\Phi = 0.075$, and dipolar coupling constants $\lambda = 0$ (black circles/line), 1 (red squares/line), 2 (green diamonds/line), 3 (blue triangles/line), and 4 (magenta crosses/line). The points are from MC simulations and the lines are from theory.

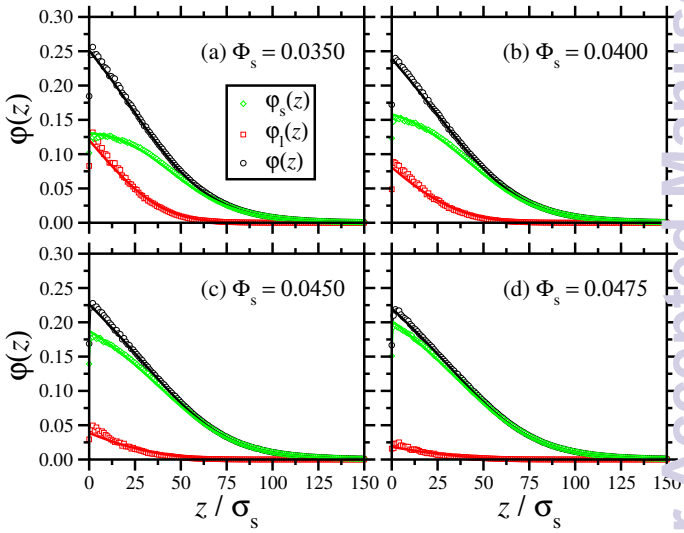

Fig. 5 Sedimentation profiles for bidisperse fluids with particle-diameter ratio $\sigma_l/\sigma_s = 1.25$, constant small-particle gravitational parameter $G_s = 0.05\sigma_s^{-1}$, $L_z = 200\sigma_s$, small-particle dipolar coupling constant $\lambda_s = 1$, and overall volume fraction $\Phi = 0.0500$. Compositions are specified by the overall small-particle volume fraction: (a) $\Phi_s = 0.0350$; (b) $\Phi_s = 0.0400$; (c) $\Phi_s = 0.0450$; (d) $\Phi_s = 0.0475$. The points are from MC simulations and the lines are from theory.

the theory does very well with the same coupling constants but at lower volume fraction, and so it must be a concentration effect instead. One possibility is that the theory underestimates the extent to which large particles separate out from the small particles at higher overall volume fraction, and this is driven by the stronger cohesive interactions between large particles, as compared to large-small and small-small interactions. Therefore, it could be that higher-order virial coefficients (from B_4 upwards) are required in order to describe important interactions within clusters of four or more (large) particles. Note that the total profile is described very well by the theory, highlighting the particular need to discriminate between small-particle and large-particle interactions.

Table 2 shows that despite the qualitative differences between the sedimentation profiles from simulation and theory, the small-particle averages $\langle\varphi\rangle_s$ and $\langle z\rangle_s$, and the total averages $\langle\varphi\rangle$ and $\langle z\rangle$, are in good general agreement. There are, though, significant differences between the large-particle averages due to the behaviour of the profiles in the region $z < 25\sigma$.

3.2 Comparison between theory and experiment

The stationary magnetic susceptibility profile $\chi(z)$ taken after 38 hours is analysed using a monodisperse model, and then a bidisperse model. To begin, the second-order modified mean-field (MMF2) theory is used to determine the apparent dipolar cou-

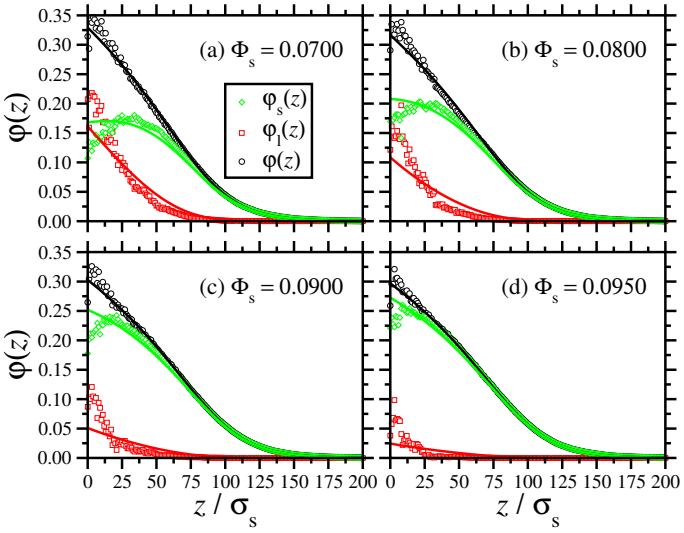

Fig. 6 Sedimentation profiles for bidisperse fluids with particle-diameter ratio $\sigma_l/\sigma_s = 1.25$, constant small-particle gravitational parameter $G_s = 0.05\sigma_s^{-1}$, $L_z = 200\sigma_s$, small-particle dipolar coupling constant $\lambda_s = 1$, and overall volume fraction $\Phi = 0.1000$. Compositions are specified by the overall small-particle volume fraction: (a) $\Phi_s = 0.0700$; (b) $\Phi_s = 0.0800$; (c) $\Phi_s = 0.0900$; (d) $\Phi_s = 0.0950$. The points are from MC simulations and the lines are from theory.

pling constant. The MMF2 expression for $\chi(z)$ is

$$\chi(z) = \chi_L(z)\left[1 + \frac{\chi_L(z)}{3} + \frac{\chi_L^2(z)}{144}\right] \qquad (18)$$

where $\chi_L(z) = 8\varphi(z)\lambda$ is the Langevin susceptibility. The MMF2 expression has been tested critically against experimental measurements and simulation results, and for ferrofluids with realistic parameters it is essentially exact. In the experiments, the system was initially homogeneous, with an overall magnetic volume fraction $\Phi^m = 0.036$ and a uniform magnetic susceptibility $\chi = 0.490$ at $T = 295$ K, which corresponds to

$$\chi_L = 8\Phi\lambda = 8\Phi^m\left(\frac{\mu_0 m^2}{4\pi k_B T x^3}\right) = 0.428. \qquad (19)$$

Taking the saturation magnetization density of magnetite to be $M_s = 4.80 \times 10^5$ A m^{-1}, these values of Φ^m and χ_L correspond to magnetite particles with magnetic-core diameter $x = 9.86$ nm. Taking the thickness of the non-magnetic oleic-acid layer to be $\delta = 2.00$ nm (a typical value) gives the hard-sphere diameter $\sigma = 13.86$ nm, the dipolar coupling constant $\lambda = 0.536$, and the volume fraction $\Phi = 0.100$. In principle, the apparent gravitational parameter as a function of z is determined from eqns. (1) and (4) to be

$$G(z) = \left(\frac{v_m \Delta\rho g}{k_B T}\right)\left[\frac{\omega^2 r(z)\cos 42^\circ}{g}\right] = G_E\left[\frac{g_c(z)}{g}\right] \qquad (20)$$

where $G_E = v_m\Delta\rho g/k_B T$ is the natural gravitational parameter on Earth, and $g_c(L_z/2) \simeq 20g$ (as stated in Section 2.1). Putting in the mass densities and the apparent particle parameters quoted above gives $G_E = 5.33$ m^{-1}. This prediction is compromised by two factors. Firstly, the oleic-acid layer on a particle does not have exactly the same mass density as the kerosene carrier liquid. Secondly, the particles experience additional friction forces from the walls of the container, and this affects the particle distribution. Therefore, the prefactor in eqn. (20) was treated as a fitting parameter in the theory, and the optimum value was determined to be $G_E = 3.63$ m^{-1} – not too dissimilar from the predicted value. The gravitational parameter in the middle of the capillary ($z = 30$ mm) is therefore $G \simeq 73$ m^{-1}, and with the apparent hard-core diameter $\sigma = 13.86$ nm, this gives a reduced gravitational parameter $G\sigma \simeq 1 \times 10^{-6}$, which is about four orders of magnitude smaller than in the MC simulations. The solution of eqn. (13) with G given by eqn. (20) yields the volume-fraction profile $\varphi(z)$ shown in Fig. 7(a). Figure 7(b) shows the corresponding magnetic-susceptibility profile $\chi(z)$ calculated from the MMF2 theory [eqn. (18)], along with the original experimental results. The agreement is very poor, the primary problem being that the theoretical curve does not rise steeply enough at small values of z. Since the theory has been shown to be accurate in Section 3.1, it must be the monodisperse model that is at fault.

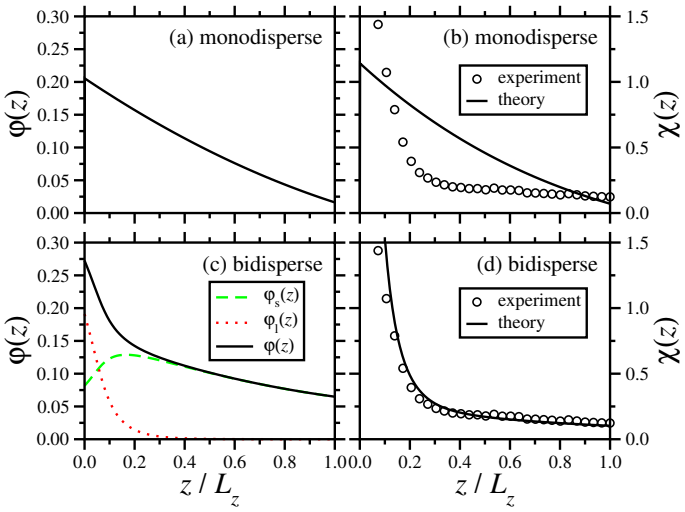

Fig. 7 Experimental and theoretical results for the volume-fraction profiles $\varphi(z)$ [(a) and (c)] and the magnetic-susceptibility profile $\chi(z)$ [(b) and (d)]. Two different models were used to fit the experimental data: a monodisperse DHS fluid [(a) and (b)]; and a bidisperse DHS fluid [(c) and (d)].

In general, it is a lengthy process to determine the full particle-size distribution without making assumptions about the number of fractions, although it can be done.[26,27] The simplest approach is to consider a bidisperse model, and in fact it has been

shown several times that the presence of small-particle and large-particle fractions is sufficient to describe polydispersity effects in real ferrofluids.[25,28,29] The gravitational parameters were obtained by scaling the monodisperse value in eqn. (20): $G_\alpha(z) = (x_\alpha/x)^3 G(z)$. The individual volume fractions and dipolar coupling constants were determined by fitting to the experimental magnetic-susceptibility profile $\chi(z)$ with the constraints

$$\chi_{\rm L} = \sum_{\alpha={\rm s,l}} 8\Phi_\alpha^{\rm m}\left(\frac{\mu_0 m_\alpha^2}{4\pi k_{\rm B}T x_\alpha^3}\right) = 0.428, \qquad (21)$$

$$\Phi^{\rm m} = \sum_{\alpha={\rm s,l}} \Phi_\alpha^{\rm m} = 0.036. \qquad (22)$$

This procedure gave the magnetic-core diameters $x_{\rm s} = 7.60$ nm and $x_{\rm l} = 14.00$ nm, and the magnetic volume fractions $\Phi_{\rm s}^{\rm m} = 0.028$ and $\Phi_{\rm l}^{\rm m} = 0.008$. Again, taking $\delta = 2.00$ nm gives the hard-core diameters $\sigma_{\rm s} = 11.60$ nm and $\sigma_{\rm l} = 18.00$ nm, the dipolar coupling constants $\lambda_{\rm s} = 0.191$ and $\lambda_{\rm l} = 2.002$, and the volume fractions $\Phi_{\rm s} = 0.099$, $\Phi_{\rm l} = 0.017$, and $\Phi = 0.116$. The volume-fraction profiles are shown in Fig. 7(c). The large-particle profile decays rapidly with height, while the small-particle profile shows a maximum at around $0.15L_z$ (similar to what was seen in the simulation profiles). Figure 7(d) shows the magnetic-susceptibility profiles from theory and experiment, and the agreement is excellent. In particular, the high concentration of large particles near the bottom of the container gives rise to a sharp increase in $\chi(z)$ there. It is stressed that the bidisperse is a minimal model of a polydisperse ferrofluid, and it is not claimed that the real ferrofluid can be resolved in to just two distinct fractions. Nonetheless, the presence of some large particles, which accumulate near the bottom of the container, does offer an explanation for the sharp rise in magnetic susceptibility observed in experiment.

As explained in Section 3.1, the presence of a maximum in the small-particle volume-fraction profile – as seen in simulations and inferred from experiment – is due to the large particles squeezing the small particles out. In the experimental system, the small particles are only weakly interacting ($\lambda_{\rm s} = 0.191$) and have a small gravitational parameter ($G_{\rm s}\sigma_{\rm s} \sim 10^{-6}$), and the large particles are strongly interacting ($\lambda_{\rm l} = 2.002$), and have a much larger gravitational parameter [because $(x_{\rm l}/x_{\rm s})^3 \simeq 6$]. In the simulated system, $\lambda_{\rm s} = 1$, $G_{\rm s}\sigma_{\rm s} = 0.05$, and $\lambda_{\rm l}/\lambda_{\rm s} = G_{\rm l}/G_{\rm s} = 1.953$. The outstanding issue is that the theory captures the maximum in $\varphi_{\rm s}(z)$ in the experimental system, but not in the simulated system at a similar overall volume fraction ($\Phi \simeq 0.1$) and with a similar composition. The orders-of-magnitude difference in gravitational parameters is not important because in both cases, $G_{\rm s}\sigma_{\rm s} << 1$. Moreover, the theory is scale-invariant, in the sense that eqn. (15) can be written in terms of new variables z/L_z and $G_\alpha L_z$, thus removing the absolute particle size from the problem. The ratio $G_{\rm l}/G_{\rm s}$ is different in the two cases, but the theory captures the gravitational contribution to the free energy exactly (assuming that Archimedes' principle holds) and so this cannot explain the inconsistency between theory and simulation. In the experiments, the gravitational parameters are functions of position, while in simulations, the parameters are constants, but in both cases peaks in $\varphi_{\rm s}(z)$ are apparent, and so this is not the cause of the discrepancy either. The significant difference is therefore in the strength of the interactions between small particles as compared to that between large particles. To demonstrate the effect of this variable, Fig. 8 shows volume-fraction profiles in bidisperse ferrofluids with the same overall volume fractions $\Phi_{\rm s} = 0.099$, $\Phi_{\rm l} = 0.017$, and $\Phi = 0.116$, and the same constant small-particle gravitational parameter $G_{\rm s} = 10L_z^{-1}$ (uniform gravitational field): in (a) $\lambda_{\rm s} = 0.191$, $\lambda_{\rm l} = 2.002$, $x_{\rm l}/x_{\rm s} = 1.84$, and $\sigma_{\rm l}/\sigma_{\rm s} = 1.55$; and in (b) $\lambda_{\rm s} = 1$, $\lambda_{\rm l} = 1.953$, and $x_{\rm l}/x_{\rm s} = \sigma_{\rm l}/\sigma_{\rm s} = 1.25$. These results show that with weakly interacting small particles, and strongly interacting large particles, a pronounced peak in $\varphi_{\rm s}(z)$ is apparent, again at around $0.15L_z$. When the small-particle and large-particle interactions are comparable, there is no small-particle peak, but in simulations with similar parameters, there is a peak. This shows that the theory – based on B_2 and B_3 – captures the difference between small-particle and large-particle interactions only when the difference between dipolar coupling constants is large. As suggested in Section 3.1, the inclusion of higher virial coefficients (B_4 and upwards) could capture the clustering behaviour of the large particles, even when the difference between dipolar coupling constants is not so large. The calculation of the third virial coefficient is already difficult enough, but numerical methods could be brought to bear on the problem,[47] as they have with other calculations on ferrofluids.[14,18]

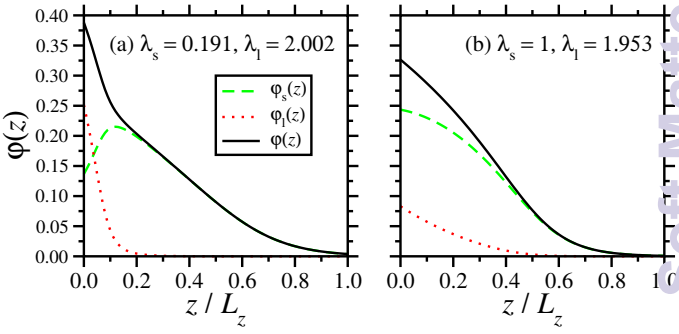

Fig. 8 Theoretical results for the volume-fraction profiles $\varphi(z)$ in bidisperse DHS fluids with equal overall volume fractions $\Phi_{\rm s} = 0.099$, $\Phi_{\rm l} = 0.017$, and $\Phi = 0.116$: (a) $\lambda_{\rm s} = 0.191$, $\lambda_{\rm l} = 2.002$, $x_{\rm l}/x_{\rm s} = 1.84$, and $\sigma_{\rm l}/\sigma_{\rm s} = 1.55$; (b) $\lambda_{\rm s} = 1$, $\lambda_{\rm l} = 1.953$, and $x_{\rm l}/x_{\rm s} = \sigma_{\rm l}/\sigma_{\rm s} = 1.25$

.

4 Conclusions

The logarithmic free energy theory has been applied to sedimentation in monodisperse and bidisperse ferrofluids. The theory has

been employed within the local-density approximation to obtain the concentration profiles of dipolar particles subject to arbitrary gravitational or centrifugal forces.

The theory has been tested critically against computer-simulation results for monodisperse and bidisperse dipolar hard-sphere fluids in strong homogeneous gravitational fields. In the monodisperse case, the comparison is excellent over broad ranges of parameters such as gravitational-field strength, volume fraction, and dipolar coupling constant. In the bidisperse case, the theory predicts the overall volume-fraction profile very accurately, but at high volume fraction (approximately 0.1 within the container overall) it does not quite capture the segregation of small and large particles near the bottom of the container observed in simulations. This segregation manifests itself in a maximum in the small-particle concentration profile, and a sharply decaying large-particle concentration profile: essentially, the large particles squeeze the small particles out from the bottom of the container. The reason why the theory fails in this one minor regard is likely due to the omission of the fourth and higher virial coefficients, which will capture the clustering of four or more large particles, and hence the displacement of small particles. Overall, these are quite stringent tests, because the simulated gravitational lengths are quite small, only 4 or 20 times the (small-)particle diameter, and in this regime one might expect the local-density approximation to break down.

The theory has been used to analyse the magnetic-susceptibility profile measured in a real ferrofluid. Theoretical concentration profiles are linked to the magnetic susceptibility profile using the highly accurate second-order modified mean-field theory. It has been shown that the assumption of monodisperse particles leads to a very poor theoretical description of the experimental results: because the theory performs so well as compared to simulations, the particle model must be at fault. The simplest possible model of a polydisperse ferrofluid is a binary mixture of particles, and with this model, the agreement between theory and experiment is excellent. The theoretical small-particle concentration profile shows a maximum, but in this case the difference between dipolar coupling constants for the small and large particles is sufficiently large to have an effect, even at the level of the second and third virial coefficients. This is demonstrated explicitly by calculating theoretical volume-fraction profiles for bidisperse ferrofluids with similar compositions and overall volume fractions, but markedly different particle diameters and dipolar coupling constants.

In summary, the logarithmic free energy approach has been applied successfully to the analysis of sedimentation in ferrofluids. Future work will be targeted towards the effects of external magnetic fields on concentration profiles in ferrofluids through the balance of gravitational, Brownian, and magnetophoretic forces.

Acknowledgements

E.A.E. and A.O.I. gratefully acknowledge research funding from the Ministry of Education and Science of the Russian Federation (Contract No. 02.A03.21.0006, Project No. 3.12.2014/K). E.V.L. and A.F.P. thank the Ural Branch, Russian Academy of Sciences for supporting Project No. 15-10-1-16. E.A.E. and P.J.C. thank the Ural Federal University for supporting collaborative visits between the Edinburgh and Ekaterinburg groups.

References

1 S. Hachisu and K. Takano, *Adv. Colloid Interface Sci.*, 1982, **16**, 233–252.
2 J.-L. Barrat, T. Biben and J.-P. Hansen, *J. Phys.: Condens. Matter*, 1992, **4**, L11–L14.
3 T. Biben, J.-P. Hansen and J.-L. Barrat, *J. Chem. Phys.*, 1993, **98**, 7330–7334.
4 T. Biben and J.-P. Hansen, *Mol. Phys.*, 1993, **4**, 853–859.
5 K. L. Planken, B. W. M. Kuipers and A. P. Philipse, *Anal. Chem.*, 2008, **80**, 8871–8879.
6 R. Piazza, S. Buzzaccaro, E. Secchi and A. Parola, *Soft Matter*, 2012, **8**, 7112–7115.
7 R. Piazza, S. Buzzaccaro and E. Secchi, *J. Phys.: Condens. Matter*, 2012, **24**, 284109.
8 R. Piazza, *Rep. Prog. Phys.*, 2014, **77**, 056602.
9 R. E. Rosensweig, *Ferrohydrodynamics*, Dover Publications, Inc., New York, 1998.
10 Q. A. Pankhurst, J. Connolly, S. K. Jones and J. Dobson, *J. Phys. D: Appl. Phys.*, 2003, **36**, R167.
11 K. L. Planken, M. Klokkenburg, J. Groenewold and A. P. Philipse, *J. Phys. Chem. B*, 2009, **113**, 3932–3940.
12 B. Luigjes, D. M. E. Thies-Weesie, A. P. Philipse and B. H. Erné, *J. Phys.: Condens. Matter*, 2012, **24**, 245103.
13 B. Luigjes, D. M. E. Thies-Weesie, B. H. Erné and A. P. Philipse, *J. Phys.: Condens. Matter*, 2012, **24**, 245104.
14 E. A. Elfimova, A. O. Ivanov and P. J. Camp, *Phys. Rev. E*, 2012, **86**, 021126.
15 A. F. Pshenichnikov, E. A. Elfimova and A. O. Ivanov, *J. Chem. Phys.*, 2011, **134**, 184508.
16 A. F. Pshenichnikov and A. A. Kuznetsov, *Magnetohydrodynamics*, 2015, **51**, 551–560.
17 J. M. Meijer, D. V. Byelov, V. Dmytro, L. R. A. Snigirev, I. Snigireva, A. P. Philipse and A. V. Petukhov, *Soft Matter*, 2013, **9**, 10729–10738.
18 E. A. Elfimova, A. O. Ivanov and P. J. Camp, *Phys. Rev. E*, 2013, **88**, 042310.
19 A. Yu. Solovyova and E. A. Elfimova, *Magnetohydrodynamics*, 2014, **50**, 237–248.
20 E. A. Elfimova, A. O. Ivanov, J. O. Sindt and P. J. Camp, *Mol.*

Phys., 2015, **113**, 3717–3728.
21 A. O. Ivanov and O. B. Kuznetsova, *Phys. Rev. E*, 2001, **64**, 041405.
22 T. Kristóf and I. Szalai, *Phys. Rev. E*, 2003, **68**, 041109.
23 T. Kristóf, J. Liszi and I. Szalai, *Phys. Rev. E*, 2004, **69**, 062106.
24 T. Kristóf, J. Liszi and I. Szalai, *Phys. Rev. E*, 2005, **71**, 031109.
25 A. O. Ivanov and S. S. Kantorovich, *Phys. Rev. E*, 2004, **70**, 021401.
26 A. O. Ivanov, S. S. Kantorovich, E. N. Reznikov, C. Holm, A. F. Pshenichnikov, A. V. Lebedev, A. Chremos and P. J. Camp, *Phys. Rev. E*, 2007, **75**, 061405.
27 A. O. Ivanov, S. S. Kantorovich, E. N. Reznikov, C. Holm, A. F. Pshenichnikov, A. V. Lebedev, A. Chremos and P. J. Camp, *Magnetohydrodynamics*, 2007, **43**, 393–400.
28 E. Novak, E. Minina, E. Pyanzina, S. Kantorovich and A. Ivanov, *J. Chem. Phys.*, 2013, **139**, 224905.
29 Yu. E. Nekhoroshkova, O. A. Goldina, P. J. Camp, E. A. Elfimova and A. O. Ivanov, *J. Exp. Theor. Phys.*, 2014, **118**, 442–456.
30 P. J. Camp, E. A. Elfimova and A. O. Ivanov, *J. Phys.: Condens. Matter*, 2014, **26**, 456002.
31 A. F. Pshenichnikov, *Instrum. Exp. Tech.*, 2007, **50**, 509–514.
32 A. F. Pshenichnikov and A. V. Lebedev, *Sov. Phys. JETP*, 1989, **68**, 498–502.
33 Yu. A. Buevich, A. Yu. Zubarev and A. O. Ivanov, *Magnitnaya Gidrodinamika*, 1989, **25**, 172–176.
34 M. S. Wertheim, *J. Chem. Phys.*, 1971, **55**, 4291–4298.
35 G. Stell, J. C. Rasaiah and H. Narang, *Mol. Phys.*, 1972, **23**, 393–406.
36 G. Stell, J. C. Rasaiah and H. Narang, *Mol. Phys.*, 1974, **27**, 1393–1414.
37 G. S. Rushbrooke, G. Stell and J. S. Høye, *Mol. Phys.*, 1973, **26**, 1199–1215.
38 L. Verlet and J.-J. Weis, *Mol. Phys.*, 1974, **28**, 665–682.
39 S. Jiang and K. S. Pitzer, *J. Chem. Phys.*, 1995, **102**, 7632–7640.
40 G. A. Mansoori, N. F. Carnahan, K. E. Starling and T. W. Leland, Jr., *J. Chem. Phys.*, 1971, **54**, 1523–1525.
41 N. F. Carnahan and K. E. Starling, *J. Chem. Phys.*, 1969, **51**, 635–636.
42 K. Aim and I. Nezbeda, *Fluid Phase Equil.*, 1983, **12**, 235–251.
43 I. Nezbeda, *Fluid Phase Equil.*, 1993, **87**, 237–253.
44 J. Kolafa and I. Nezbeda, *Fluid Phase Equil.*, 1994, **100**, 1–34.
45 I. Nezbeda and W. R. Smith, *Fluid Phase Equil.*, 2004, **216**, 183–186.
46 J. Krejčí and I. Nezbeda, *Fluid Phase Equil.*, 2012, **314**, 156–160.
47 J. K. Singh and D. A. Kofke, *Phys. Rev. Lett.*, 2004, **92**, 220601

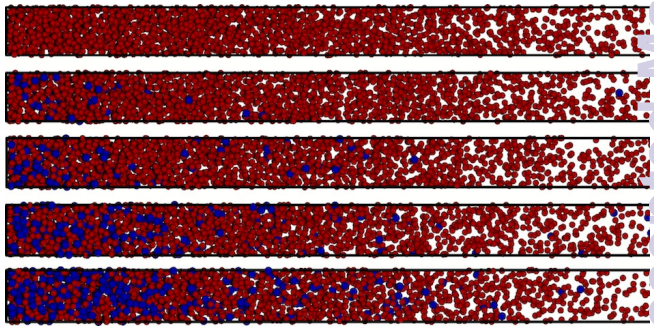

TOC Graphic: An accurate theory of sedimentation in polydisperse ferrofluids is developed and tested against experimental and simulation results.